Earth and Space Science

RESEARCH ARTICLE
10.1029/2018EA000477

Key Points:
- An innovative method is developed to analyze Cassini UVIS stellar occultation observations
- Abundances of major hydrocarbon and nitrile species are derived from observations during a flyby with large instrument pointing motion
- The new method allows exploration of Titan's upper atmosphere over seasons, latitudes, and longitudes

Supporting Information:
- Supporting Information S1
- Figure S1
- Figure S2
- Figure S3
- Figure S4
- Figure S5
- Data Set S1
- Data Set S2

Correspondence to:
S. Fan,
stfan@gps.caltech.edu

Citation:
Fan, S., Shemansky, D. E., Li, C., Gao, P., Wan, L., & Yung, Y. L. (2019). Retrieval of chemical abundances in Titan's upper atmosphere from Cassini UVIS Observations with pointing motion. *Earth and Space Science*, *6*. https://doi.org/10.1029/2018EA000477

Received 18 SEP 2018
Accepted 8 MAY 2019
Accepted article online 22 MAY 2019

Retrieval of Chemical Abundances in Titan's Upper Atmosphere From Cassini UVIS Observations With Pointing Motion

Siteng Fan[1], Donald E. Shemansky[2], Cheng Li[1], Peter Gao[3], Linfeng Wan[4], and Yuk L. Yung[1,5]

[1]Division of Geological and Planetary Sciences, California Institute of Technology, Pasadena, CA, USA, [2]Space Environment Technologies, Altadena, CA, USA, [3]Department of Astronomy, University of California, Berkeley, CA, USA, [4]Department of Earth and Planetary Sciences, University of California, Santa Cruz, CA, USA, [5]Jet Propulsion Laboratory, California Institute of Technology, Pasadena, CA, USA

Abstract Cassini/Ultraviolet Imaging Spectrograph (UVIS) Far-UV observations of stellar occultations at Titan are well suited for probing its atmospheric composition and structure. However, due to instrument pointing motion, only 5 out of tens of observations have been analyzed. We present an innovative retrieval method that corrects for the effect of pointing motion by forward modeling the Cassini/UVIS instrument response function with the pointing motion value obtained from the SPICE C-kernel along the spectral dimension. To illustrate the methodology, an occultation observation made during flyby T52 is analyzed, when the Cassini spacecraft had insufficient attitude control. A high-resolution stellar model and an instrument response simulator that includes the position of the point source on the detector are used for the analysis of the pointing motion. The Markov chain Monte Carlo method is used to retrieve the line-of-sight abundance profiles of eleven species (CH_4, C_2H_2, C_2H_4, C_2H_6, HCN, C_4H_2, C_6N_2, C_6H_6, haze, HC_3N, and C_2N_2) in the spectral vector fitting process. We obtain tight constraints on all of the species aside from C_2H_6, C_2N_2, and C_6N_2, for which we only retrieved upper limits. This is the first time that the T52 occultation was used to derive abundances of major hydrocarbon and nitrile species in Titan's upper and middle atmosphere, as pointing motion prohibited prior analysis. With this new method, nearly all of the occultations obtained over the entire Cassini mission could yield reliable profiles of atmospheric composition, allowing exploration of Titan's upper atmosphere over seasons, latitudes, and longitudes.

1. Introduction

Stellar occultation observations made by the Cassini Ultraviolet Imaging Spectrograph (UVIS; Esposito et al., 2004) are essential for constraining the photochemistry of Titan's upper atmosphere, where hydrocarbon and nitrile species show spectral features in the ultraviolet (Hörst, 2017). During the last decade, vertical profiles of these species have been derived from selected Titan flybys (Kammer et al., 2013; Koskinen et al., 2011; Liang et al., 2007; Shemansky et al., 2005), which have increased our understanding of physical and chemical processes in Titan's atmosphere. Far-UV (FUV) observations are especially important in constraining the abundances of hydrocarbons more complex than methane, as well as nitriles. However, FUV observations from only 5 (TB, T21, T41i, T41e, and T53) out of the tens of flybys have been used for retrievals to date (Capalbo et al., 2016; Koskinen et al., 2011; Shemansky et al., 2005) due to instrument pointing motion, which causes movement of the stellar image on the UVIS detector. Pointing motion is introduced by the spacecraft attitude control system, which frequently triggers thrusters during occultation observations (Chiang et al., 1993). Deadband of attitude control during stellar occultations is set as ± 0.5 mrad (Pilinski & Lee, 2009), comparable to that of a spectral pixel (1.0 mrad $\times$ 0.25 mrad), which leads to a shift in the spectral structure. Consequently, the traditional method of analyzing extinction spectra obtained by dividing the nonzero optical depth target spectrum by the extinction-free target spectrum becomes inaccurate. The spectral distortion is nonlinear due to UVIS internal instrument scattering. Attempts have been made to determine pointing motions for other instruments, for example, Cassini/VIMS (Maltagliati et al., 2015), and similar issues arose for similar UV instruments when observing stellar occultations of Titan's atmosphere (e.g., Voyager 1 UVS, Vervack et al., 2004). Using an instrument simulator for forward modeling is essential for evaluating spectra.

10.1029/2018EA000477

Table 1
Stellar Occultation During T52

	Start	Near 1,000 km	Near 500 km	End
Time	2009-093 23:55:27	2009-094 00:10:51	2009-094 00:16:51	2009-094 00:27:49
Latitude (°)	32.6	35.6	37.1	39.1
Longitude (°)	328.9	319.5	312.8	292.7
Ray Height (km)	2347	999	502	-290

Note. Latitude and longitude are computed for the impact parameter (radial vector from body center). It varied by a few degrees during the observation due to spacecraft motion.

Our proposed method uses a Cassini/UVIS simulator for forward modeling that combines the pointing information obtained from the SPICE C-kernel (NASA NAIF) and line-of-sight (LOS) chemical abundances in Titan's atmosphere to simulate spectra. The Markov chain Monte Carlo (MCMC) method (Foreman-Mackey et al., 2013) is used as the parameter search tool. Using our proposed method, we derive for the first time vertical profiles of hydrocarbon and nitrile species from flyby T52, which shows significant pointing motion during the entire duration of the observation.

The remainder of this paper is organized as follows: In section 2, the pointing motion during flyby T52 and its effects are demonstrated; detailed methodology is presented in section 3; analysis of synthetic spectrum for method testing is in section 4; spectral analysis results and vertical profiles of retrieved species are given in section 5, together with brief discussions; and our conclusions and the implications for applying this method are discussed in section 6.

2. Compensating for Pointing Motion

The instrument used in this work is the Cassini/UVIS FUV spectrograph. It covers the spectral range between 1,115 and 1,912 Å (Esposito et al., 2004). We select flyby T52 for demonstrating our new retrieval method, which took place on 3 April 2009, with the stellar source α Eri. The occultation observation during this flyby is divided into two segments due to different integration durations. We analyze the second segment (NASA PDS ID: FUV2009_093_23_55) in this work, which has an integration duration of 1.75 s for each image; the ray tangent height of incoming stellar light above Titan's surface during this segment was within the critical range (0-1,500 km) for atmospheric characterization. The geometry of this segment is given in Table 1, computed from the SPICE C-kernel (NASA NAIF).

The image of α Eri is a point source compared to the pixel size on the slit. Five spatial pixels with indices 25 to 29 were electronically windowed to record the photon counts. Each pixel has a length of 1.0 mrad along the spatial dimension (length from upper left to lower right in Figure 1a) and the low resolution slit width was set to 1.5 mrad (width from upper right to lower left in Figure 1a). During the stellar occultation, the spacecraft navigation system controls pointing through a stellar/solar referenced 3-axis stabilized platform with a deadband of 0.5 mrad referenced to the UVIS FUV principal axis (Pilinski & Lee, 2009). The thrusters of the spacecraft attitude control system react only at the deadband limit. Therefore, the star image shows motion on the slit (green line in Figure 1a), which results in changes in photon count distributions among spatial pixels along the spatial dimension and spectrum distortions along the spectral dimension. The effect of star image motion along the spatial dimension can be eliminated by summing up the photon counts received by all five spatial pixels after flat fielding. The windowed spatial pixels fully contain the stellar image during the entire T52 occultation. Motion of the star image along the spectral dimension, however, must be modeled to analyze the data, which is the focus of this work.

The star image position on the slit along the spectral dimension as a function of the ray tangent height in Titan's atmosphere during T52 is shown in Figure 1b. The star image moved at a constant rate within ±0.5 mrad between the deadband points, showing nominal function of the control system. This introduces strong distortions in the spectral dimension, as demonstrated in Figure 1c by the simulated spectra with different pointing motions. An extinction feature of C_2H_2 near 1,520 Å is shifted by a few pixels due to the pointing motion, causing a difference in spectral structure between spectra that prevents constructing extinction spectra by dividing one spectrum by another. Moreover, due to the photon scattering effects in the instrument, a single spectral line is spread across a wide range of wavelengths, necessitating simultaneous modeling of a large swath of the spectrum. The full width at half maximum of a typical spectral line is ~1.5 Å, or approximately two spectral pixels, while the line wings extend hundreds of angstroms. This results in nonlinearity in the spectrum. Figure 1d shows an example of internal photon scattering. Photon counts shortward of 1,360 Å are mostly the result of internal scattering from longer wavelengths when CH_4 extinction saturates this range. Therefore, it is not feasible to shift the spectrum back even if the value

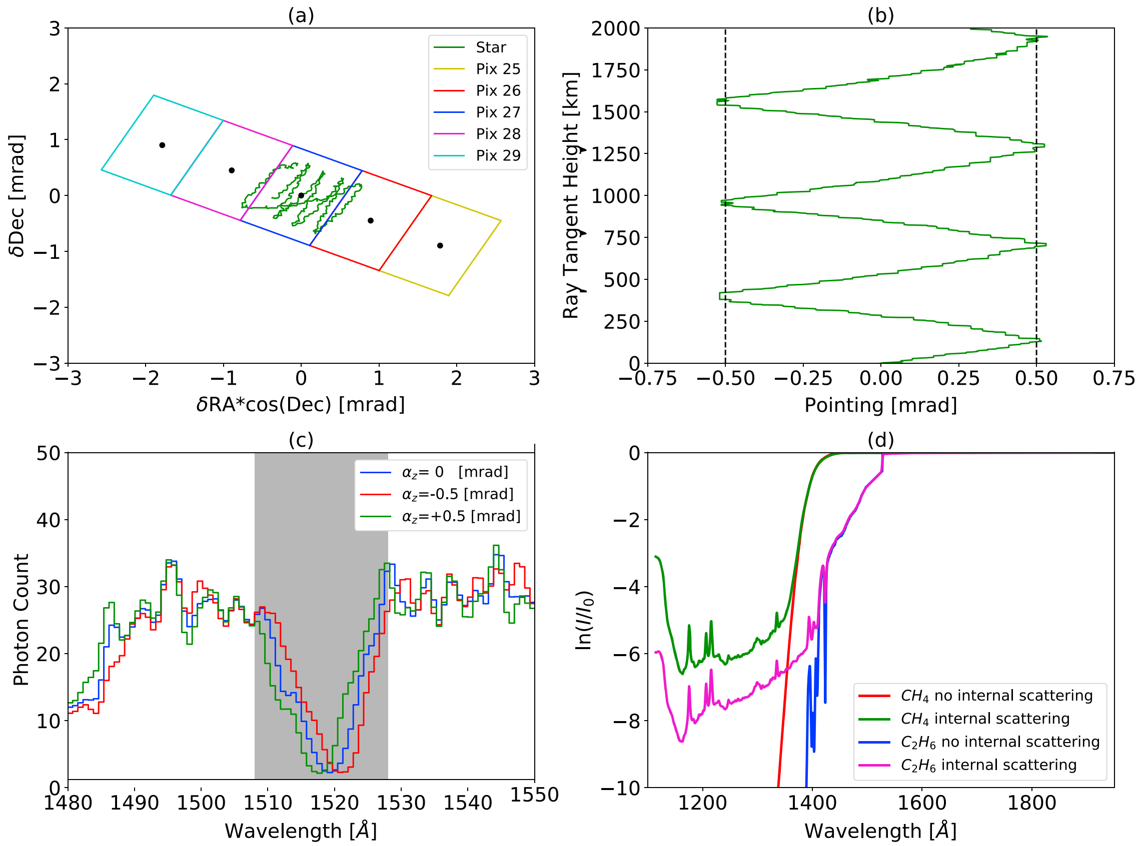

Figure 1. Pointing motion and its effects. (a) Spatial orientation of Cassini/Ultraviolet Imaging Spectrograp detector pixels (color rectangles) with their centers (black points) and the star motion on the detector (green solid line) obtained from the SPICE C-kernel. The pixel with index 27 (blue rectangle) is the center pixel during the T52 occultation observation. The spatial dimension is along the length of the 5 pixels, with the spectral dimension being perpendicular to that. (b) Vertical profile of pointing motion above Titan's surface along the spectral dimension (solid green line). Deadbands along this dimension at each end are denoted by two vertical black dashed lines. (c) Simulated photon count spectra from the T52 occultation at 754-km ray tangent height with pointing values along the spectral dimension of 0 (blue), -0.5 (red) and +0.5 mrad (green). The shaded area indicates the signature extinction feature of C_2H_2 near 1,520 Å. Figure S1 shows the full extent of the three spectra in the far-ultraviolet wavelength range. (d) Extinction spectra of CH_4 and C_2H_6 with (green for CH_4 and magenta for C_2H_6) and without (blue for CH_4 and red for C_2H_6) taking into account instrument internal scattering. The line-of-sight abundances for both species are set to 10^{18} cm^{-2}, which is approximately the value for that of CH_4 at 750 km.

of the pointing motion were known. A forward instrument model is essential for extracting information from these distorted spectra.

3. Methodology

A detailed description of Cassini/UVIS data calibration and reduction is given in chapters 9 and 10 of the Cassini/UVIS Users Guide, available in NASA-PDS (2017). To improve statistical accuracy, spectra obtained during T52 are integrated over time intervals of 17.5 s, covering an altitude range of ~25 km. The selected integration intervals are merged with pointing information obtained from the SPICE C-kernel (NASA NAIF), which is shown in Figure 1b as the green path. The reference spectrum of the star (I_0) is constructed by averaging the spectra when the ray tangent height is greater than 1,500 km above Titan's surface, where extinction by Titan's atmosphere is negligible and the pointing motion is less than 0.125 mrad (half of a pixel width).

Our forward model combines an extinction model and an instrument simulator. The extinction model computes the intensity spectrum received by Cassini/UVIS, while the instrument simulator (Shemansky et al., 2005; Shemansky & Liu, 2012) generates photon count observations based on the intensity spectrum, instrument internal scattering, and pointing motion. The instrument simulator contains high-resolution response functions for each pixel, which encapsulate the effects of instrument internal scattering that were measured

Table 2
Extinction Cross-Sections

Species	Reference	Wavelengths (Å)
CH_4	Kameta et al. (2002)	1,115-1,426
	Chen and Wu (2004)	1,426-1,490
C_2H_2	Wu et al. (2001)	1,115-1,912
C_2H_4	Wu et al. (2004)	1,115-1,912
C_2H_6	Au et al. (1993)	1,115-1,193
	Wu et al. (2004)	1,199-1,528
HCN	Nuth and Glicker (1982)	1,115-1,300
	Lee (1980)	1,300-1,568
C_4H_2	Ferradaz et al. (2009)	1,150-1,912
C_6N_2	Connors et al. (1974)	1,115-1,912
C_6H_6	Pantos et al. (1978)	1,115-1,912
HC_3N	Ferradaz et al. (2009)	1,150-1,560
C_2N_2	Nuth and Glicker (1982)	1,115-1,701

in the lab and calibrated in flight. The core of the point spread function has a full width at half maximum of ~1.7 Å, and the wings extend over a spectral range of 800 Å.

Eleven hydrocarbon and nitrile species (CH_4, C_2H_2, C_2H_4, C_2H_6, HCN, C_4H_2, C_6N_2, C_6H_6, haze, HC_3N, and C_2N_2), which have extinction features in the FUV, are considered in the forward model. We include two species in the retrieval, C_2N_2 and C_6N_2, which have not been detected previously, to examine the extent to which their abundances can be constrained, as photochemical models suggest their existence (e.g., Willacy et al., 2016). The cross-sections of these species are obtained from laboratory work (Table 2), some of which were conducted at room temperature. The differences in temperatures between that of the measurements and ambient conditions in Titan's atmosphere may contribute ~20% uncertainty to the LOS abundances. Pressure effects are negligible. Haze particles are assumed to be spherical with a radius of 12.5 nm and the same optical properties as their laboratory analogs ("tholin"; Khare et al., 1984), in line with Liang et al. (2007) and Koskinen et al. (2011). We combine the LOS abundances and cross-sections to construct spectra based on a normalized I_0.

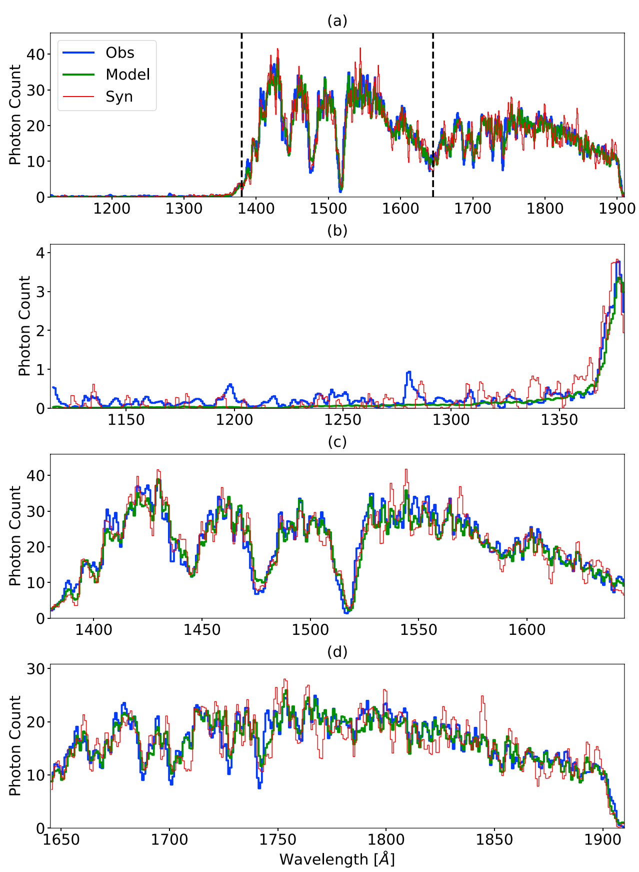

Figure 2. (a) Photon count spectra of the T52 occultation at 754-km ray tangent height showing the observed spectrum (blue), the best fit simulated model spectrum (green), and the synthetic spectrum (red), which includes artificially introduced noise. (b–d) Detailed views of the photon count spectra split along the black dashed lines in (a). The *y* axis scales are different in (b)–(d) for the purpose of presentation. The spectral contribution of each species to this spectrum is shown in Figure S2.

Retrieval is a multivariable inverse problem. Combining a proper retrieval algorithm with a forward model, physical properties can be derived from the observations. The MCMC method is used in this work to solve the inverse problem. It searches parameter space with the ability to extract asymmetric posterior probability density functions (PDFs) in a computationally feasible way. For each proposed parameter set, a spectrum is constructed with the procedure described above and is then compared with the observed spectrum to determine the posterior probability of this parameter set. The cost function is defined as follows:

$$\ln(p) = -\frac{1}{2}\sum_i \left[\frac{\left(I_{Obs_i} - I_{MCMC_i}\right)^2}{\sigma_i^2 + 0.1} + \ln\left(\sigma_i^2 + 0.1\right)\right],$$

where p is the posterior probability of one proposed parameter set; I_{Obs} and I_{MCMC} are the photon counts from the observation and those calculated from the forward model during one MCMC attempt, respectively; and σ_i is the standard deviation of the spectral intensity at wavelength i, assumed to be the square root of the simulated photon count. A softening factor of 0.1 is added to the standard deviation at each wavelength to avoid dividing by zero when the intensity decreases to zero at some wavelengths at low altitudes. An example of I_{Obs} and I_{MCMC} is shown in Figure 2 as blue and green lines, respectively. With this cost function, we use the emcee package (Foreman-Mackey et al., 2013) to conduct the MCMC parameter search. An MCMC procedure with 120 chains, selected according to the number of parameters, is used to search through parameter space. A bounded uniform prior in log space is set for each parameter, so abundances are retrieved with no prior knowledge within 2 orders of magnitude of the predicted values from the latest results of the Caltech/JPL photochemical model KINETICS (Li et al., 2014; Li et al., 2015; Willacy et al., 2016). The bounds are adjusted by 2 orders of magnitude if necessary after each 2,000 steps according to the PDF of the parameter and the converging criterion. The MCMC procedure is extended for 2,000 more steps after the final bound adjustment to generate the resulting PDFs.

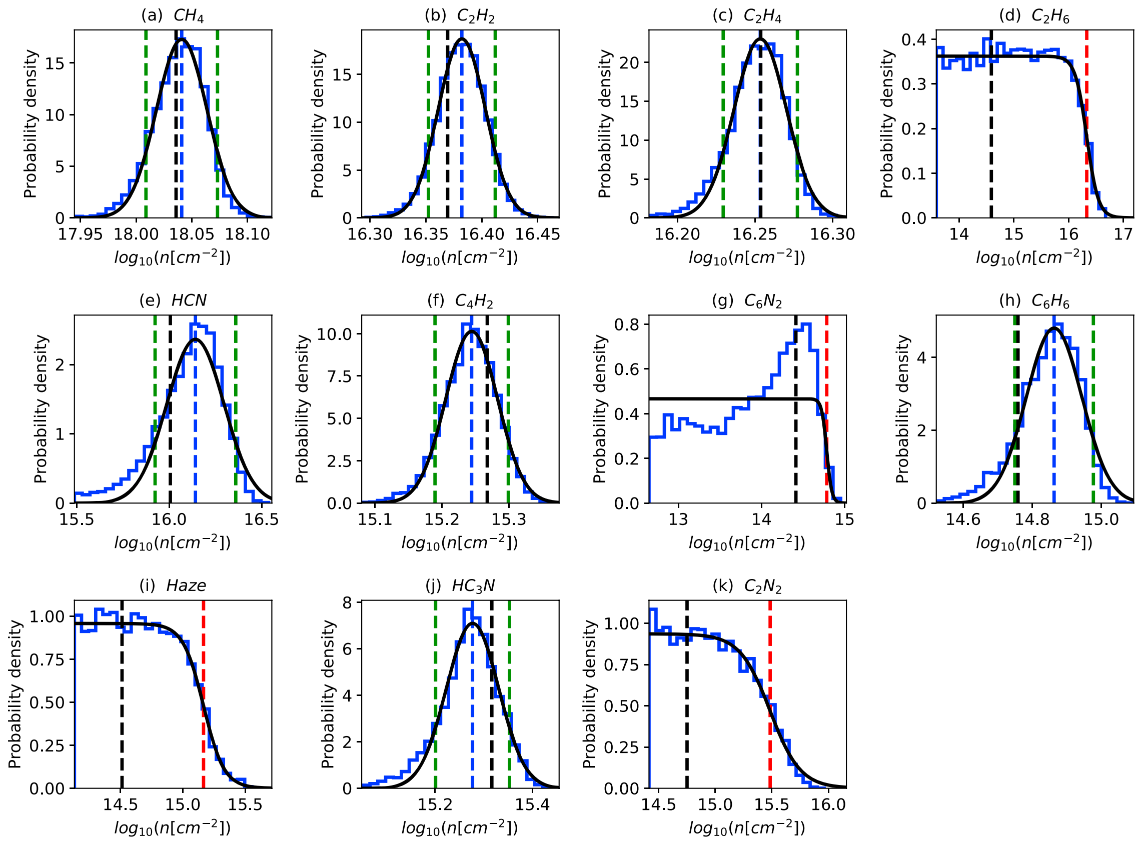

Figure 3. Probability density functions (blue solid lines) of the logarithm of line-of-sight abundances of (a) CH_4, (b) C_2H_2, (c) C_2H_4, (d) C_2H_6, (e) HCN, (f) C_4H_2, (g) C_6N_2, (h) C_6H_6, (i) haze, (j) HC_3N, and (k) C_2N_2 retrieved from the synthetic spectrum (red line in Figure 2). The black dashed lines indicate the line-of-sight abundances used to generate the synthetic spectrum, that is, the "true" value. The best fit function to each probability density function (Gaussian, sigmoid, or constant) is shown as black solid lines. The median and 1σ confidence interval are denoted by blue and green dashed lines, respectively, for well-constrained species. For others, the upper limits are denoted by red dashed lines. The correlations among the parameters are shown in Figure S3.

4. Synthetic Spectrum Analysis

We analyze a synthetic spectrum (red line in Figure 2) to test the reliability of our method. We use the LOS abundances of all species obtained from fitting to the observation (green line in Figure 2) as well as the pointing motion (Figure 1b) to construct the initial synthetic spectrum. We then add noise on the level of the square root of the simulated photon count plus the softening factor to obtain the final synthetic spectrum (red line in Figure 2) with the same calibration procedure as the data. In other words, the synthetic spectrum is the same as the simulated spectrum used to fit the observations, except it includes noise. Figure 2 shows that the noise level is slightly greater than the disagreements between the simulated spectrum and the observation, such that the analysis of the synthetic spectrum should give a lower limit to the reliability of our method.

Figure 3 shows the PDFs of the LOS abundances of hydrocarbon and nitrile species resulting from the synthetic spectrum analysis. The LOS abundance values used to construct the synthetic spectrum are shown as black dashed lines. The constraint on each LOS abundance is interpreted by fitting the PDFs with three types of functions: Gaussian, sigmoid, and constant, and the PDFs are categorized as such by comparing the residuals of the fit. LOS abundances with Gaussian-like PDFs are defined as well constrained (e.g., CH_4, C_2H_2, C_2H_4, HCN, C_4H_2, C_6H_6, and HC_3N in Figure 3). These species typically have distinct spectral features (Figure S2) that allow for strong constraints. The retrieved LOS abundances of these species are all within ~1σ of the true values, indicating that our retrieval method is stable to random noise. The LOS abundance PDFs of some other species (e.g., C_2H_6, C_6N_2, haze, and C_2N_2 in Figure 3) show asymmetric behavior and so can only provide upper limits through fits to the sigmoid function. Interestingly, ethane (C_2H_6), one of the major hydrocarbons, belongs in this category due to overlapping spectral features with the most

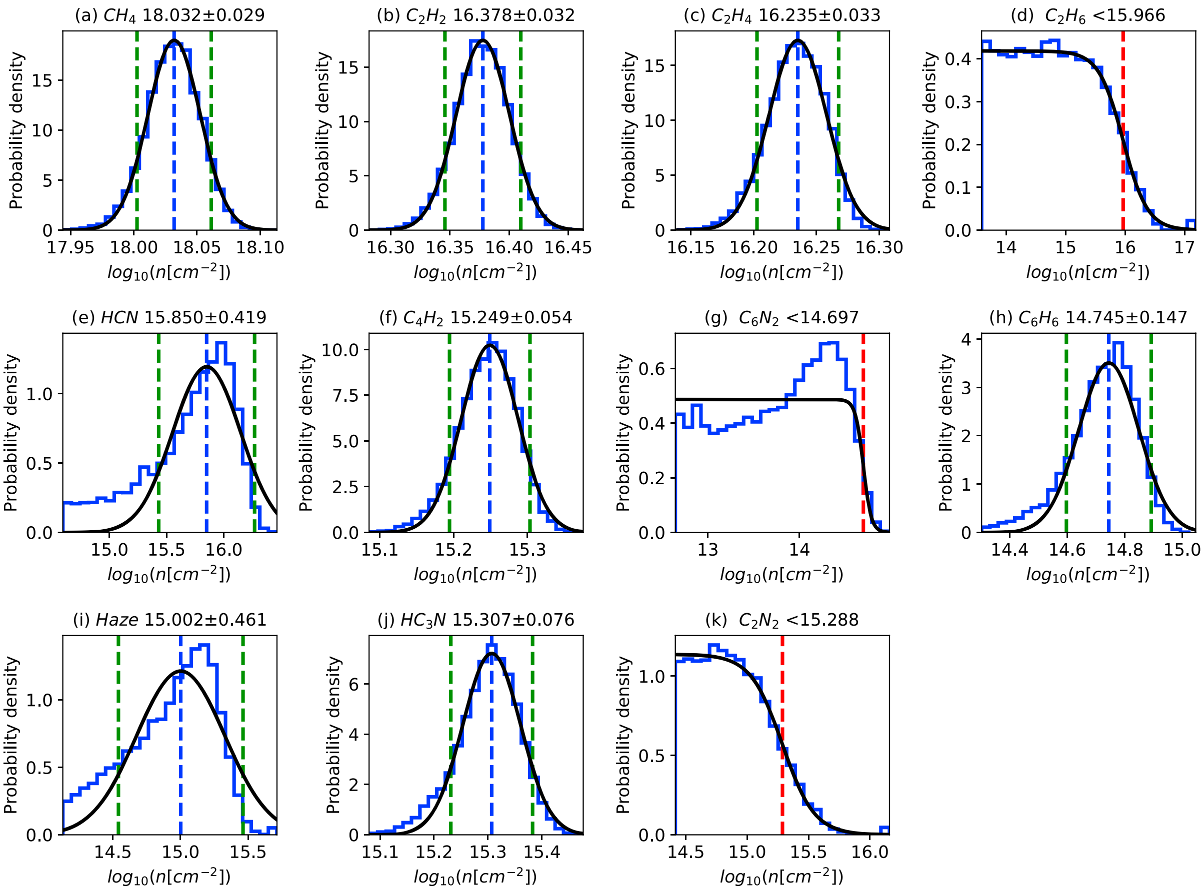

Figure 4. Probability density functions of the logarithm of line-of-sight abundances of (a) CH_4, (b) C_2H_2, (c) C_2H_4, (d) C_2H_6, (e) HCN, (f) C_4H_2, (g) C_6N_2, (h) C_6H_6, (i) haze, (j) HC_3N, and (k) C_2N_2 retrieved from a photon count spectrum at 754-km ray tangent height (blue solid lines). The best fit function to each probability density function (Gaussian, sigmoid, or constant) is shown as black solid lines. The median and 1σ confidence interval are denoted by blue and green dashed lines, respectively, for well-constrained species. For others, the upper limits are denoted by red dashed lines. The medians, 1-σ confidence intervals, and upper limits are also given atop each subplot. The correlations among the parameters are shown in Figure S4.

abundant hydrocarbon, methane (CH_4, Figure 1d), whose LOS abundance is 2 orders of magnitude higher, resulting in the anticorrelation of these two PDFs (Figure S3). The failure to retrieve ethane is consistent with previous results obtained above 700 km during flyby T41i (Koskinen et al., 2011). In some cases, the PDFs may be between Gaussian and sigmoid, such as that of C_6N_2 in this analysis, which shows a peak with poorly constrained lower limits; as the type of PDF is still determined by the value of the residuals, the case of C_6N_2 and others like it would either have only upper limits (more sigmoid-like) or be constrained with relatively large uncertainties (more Gaussian-like).

5. Results and Discussion

An example spectrum from the T52 occultation observation at ~750 km is shown in Figure 2, together with a simulated spectrum that best fits the observation. PDFs for the LOS abundances of hydrocarbon and nitrile species resulting from retrievals of this spectrum are shown in Figure 4. Most of the behavior of these PDFs are consistent with those in Figure 3. Six species (CH_4, C_2H_2, C_2H_4, C_4H_2, C_6H_6, and HC_3N) show Gaussian-like PDFs and are thus well constrained with precise values for the LOS abundances and small uncertainties. It is worth noting that the uncertainties shown here are only from photon noise; another probable source of uncertainties is the presently unavailable temperature dependencies of extinction cross-sections, which may introduce systematic errors. Three other species (C_2H_6, C_6N_2, and C_2N_2) have asymmetric PDFs more similar to the sigmoid function, with only well-defined upper limits. HCN and haze both have PDFs that are close to Gaussian and as such are categorized as well constrained, but with large uncertainties (about a factor of 3). The third PDF type, a constant, is not shown in either Figure 3 or 4, as all retrieved species are

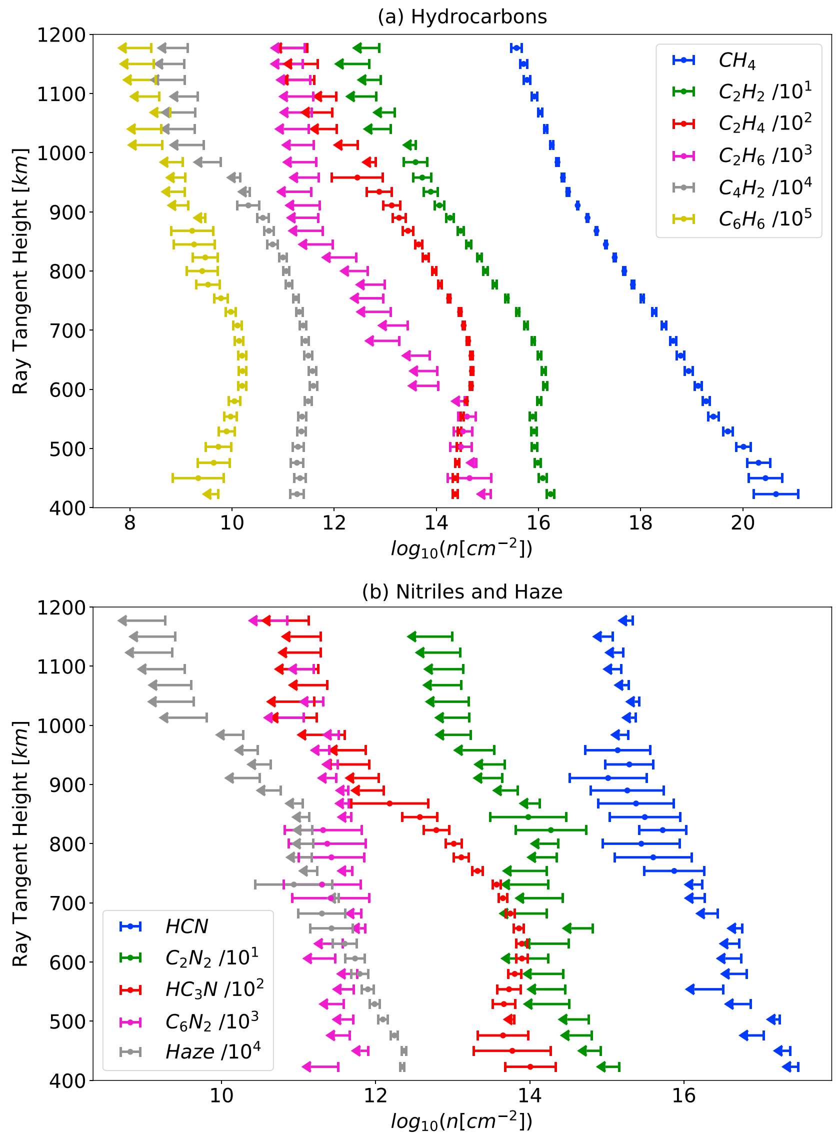

Figure 5. Vertical profiles of the logarithm of line-of-sight abundances of (a) hydrocarbons and (b) nitriles and haze retrieved from T52 occultation observations. Some species are offset by a few orders of magnitude for the purpose of presentation. Points with error bars denote well-constrained values, while arrows denote upper limits. The lengths of the arrows denote the width of each soft upper limit threshold. Haze particles are assumed to be 12.5-nm spheres with the same optical properties as their laboratory analog ("tholin"; Khare et al., 1984). Data used to generate this figure are available in the supporting information. Comparison of line-of-sight abundances of CH_4, C_2H_2, C_2H_4, and HCN with two previous flybys (TB and T41i) is given in Figure S5.

constrained to some extent at ~750 km. A constant PDF usually takes place only when the ray tangent height is either too high or too low in the atmosphere, where the LOS abundances of some species are either insufficient to be seen or overwhelmed by saturated absorption, respectively. In other words, flat PDFs would be returned when there is almost no information in the spectrum.

Repeating the procedures outlined above for all available altitudes, we present the vertical profiles of LOS abundances of all eleven species in Figure 5 with error bars and arrows for well-defined constraints and upper limits, respectively. This is the first time that the LOS abundance profiles of these species are retrieved from a flyby with significant pointing motion. Comparison of the CH_4, C_2H_2, C_2H_4, and HCN profiles with those retrieved from the TB (Shemansky et al., 2005) and T41i flybys (Koskinen et al., 2011) is given in Figure S5. It shows general agreement between these three retrievals despite some differences at higher altitudes, which may result from the different seasons and/or latitudes. Among the major hydrocarbons

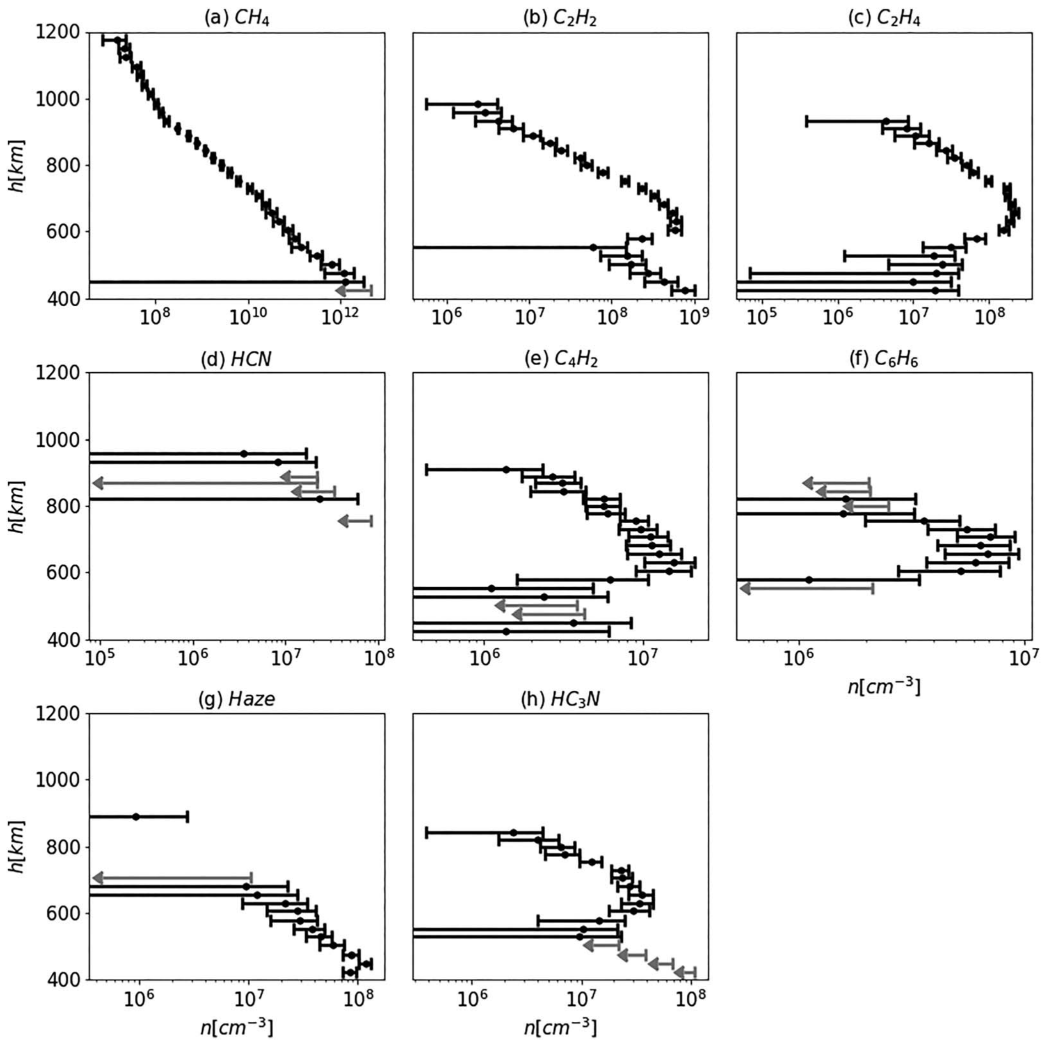

Figure 6. Number density profiles of (a) CH_4, (b) C_2H_2, (c) C_2H_4, (d) HCN, (e) C_4H_2, (f) C_6H_6, (g) haze, and (h) HC_3N retrieved from T52 occultation observations. Black points with error bars denote well-constrained values, while gray arrows denote upper limits. The lengths of the arrows denote the width of each upper limit soft threshold. Haze particles are assumed to be 12.5-nm spheres with the same optical properties as their laboratory analog ("tholin"; Khare et al., 1984). Data used to generate this figure are available in the supporting information.

(Figure 5a), only the most abundant species, CH_4, is detectable above 1000 km, while all the others only exhibit upper limits. With decreasing altitude, concentrations of larger organic molecules increase due to photochemistry. All of the major hydrocarbons except C_2H_6 remain well constrained down to 400 km, where absorption saturates. Spectral features of C_2H_6 overlap with that of CH_4 for most of the altitude range, resulting in a failure to retrieve its abundance, as discussed in section 4. Among nitriles, HCN is constrained with relatively large uncertainties between 700 and 1,000 km, while HC_3N is well constrained to much lower altitudes. Only upper limits for C_6N_2 and C_2N_2 are obtained, so we do not claim a detection. Tighter constraints may be obtained from spectra with higher signal-to-noise ratio measured during a more stable flyby (e.g., T41i), which we will investigate in a future publication. Aside from the major hydrocarbon and nitriles, our new method can also identify the two long wavelength absorbers, benzene and haze. Benzene is well constrained below 900 km due to its distinguishable feature near 1,790 Å, while haze particles can only be retrieved below 750 km. The range of altitudes where haze is well constrained in our work is smaller than those of Liang et al. (2007) and Koskinen et al. (2011). Liang et al. (2007) retrieved the haze profile up to 1,000 km from observations obtained during flyby TB by assuming that all extinction between 1,850 and 1,900 Å is caused by haze, as benzene was not included as a potential absorber. However, the current work shows that benzene can contribute up to 50% of the extinction in this wavelength range, so the ambiguity of the two absorbers needs to be considered.

Koskinen et al. (2011) also retrieved the haze profile up to 1,000 km using observations obtained during two stable flybys T41i and T53, while assuming that the PDF of the LOS abundance of haze was Gaussian. Both the higher signal-to-noise ratio of these observations and the assumption of a Gaussian PDF could have contributed to a greater altitude range where haze LOS abundance can be constrained. Applying our method to these flybys may help to understand why these differences exist.

LOS abundances of eight species (CH_4, C_2H_2, C_2H_4, HCN, C_4H_2, C_6H_6, haze, and HC_3N) are converted to number density profiles to allow for ease of comparison to photochemical models. Three species (C_2H_6, C_2N_2, and C_6N_2) are excluded, as their LOS abundances are not well constrained over most of the considered altitude range. The Abel inverse transform is used here, which assumes spherical symmetry, to compute the vertical profiles. A Bootstrap Monte Carlo (BSMC) method is used to evaluate the quality of conversion and provide uncertainties. BSMC has the advantage of being applicable to different types of PDFs of the LOS abundances, which is necessary since a number of the PDFs are not Gaussian. The number density profiles of each species are computed individually since each species is independent of others. In each computation, a set of LOS abundances at all retrieving altitudes for the given species is sampled from their PDFs (e.g., one of the panels in Figure 4) at each BSMC step, from which we compute the corresponding vertical number density profile. As the distribution of species LOS abundances in the Markov chains obtained from the retrieval are identical to their PDFs when the MCMC procedure reaches equilibrium, we used the values in the last 1,500 steps of each of the 120 chains as the sampling procedure for BSMC and generate 180,000 number density profiles for each species. Therefore, at each altitude of an individual species, we obtain 180,000 probable number densities, which form a number density PDF. To interpret these PDFs, we use the same method of fitting them with three types of functions (Gaussian, sigmoid, and constant) and categorized them by comparing the residuals as mentioned in section 4. Number density profiles corresponding to well-constrained number densities and upper limits with positive values are shown in Figure 6. As the number density at each altitude is computed with contributions from both well and poorly constrained LOS abundances, the number densities have larger relative uncertainties and smaller ranges of altitudes where they are well constrained. Major hydrocarbons with large abundances and distinct spectral features (CH_4, C_2H_2, and C_2H_4; Figures 6a–6c) are well constrained over a wide range of altitudes. In contrast, the number density of the most abundant nitrile, HCN, is poorly constrained for most of the altitude range considered (Figure 6d) due to its large LOS abundance uncertainty (Figure 5b). Other minor species (Figure 6e-6h) are well constrained over at least some of the considered altitude range and can thus provide constraints on Titan's atmospheric chemistry.

6. Conclusions

A new method to correct for the effects of pointing motion of Cassini/UVIS has been developed using an instrument simulator and the MCMC method. The new approach is successfully applied to the T52 stellar occultation observations of Titan's atmosphere to retrieve the LOS abundances and number densities of hydrocarbon and nitrile species and allows for the quantification of how well each LOS abundance and number density can be constrained, facilitating the analysis of all Cassini/UVIS stellar occultations at Titan. Application of the present method to all available observations is expected to reveal seasonal and latitudinal variations in the atmospheric composition of Titan, thereby providing useful constraints for photochemical and global circulation models.

Acknowledgments
This research was supported in part by the Cassini/UVIS program via NASA Grant JPL.1459109 to the California Institute of Technology and was partially supported by funding from NASA's Astrobiology Institute's proposal “Habitability of Hydrocarbon Worlds: Titan and Beyond” (PI R.M. Lopes). All the data and tools in this work are publicly available. Cassini/UVIS data are available on NASA PDS (pds.nasa.gov). The python package emcee is available online (dfm.io/emcee/current). We thank Tommi T. Koskinen and Karen Willacy for sharing results.

References

Au, J. W., Cooper, G., Burton, G. R., Olney, T. N., & Brion, C. E. (1993). The valence shell photoabsorption of the linear alkanes, C_nH_{2n+2} (n=1–8): Absolute oscillator strengths (7–220 eV). *Chemical Physics*, *173*, 209–239. https://doi.org/10.1016/0301-0104(93)80142-V

Capalbo, F. J., Benilan, Y., Fray, N., Schwell, M., Champion, N., Es-sebbar, E., et al. (2016). New benzene absorption cross sections in the VUV, relevance for Titan's upper atmosphere. *Icarus*, *265*, 95–109. https://doi.org/10.1016/j.icarus.2015.10.006

Chen, F. Z., & Wu, C. Y. R. (2004). Temperature-dependent photoabsorption cross sections in the VUV-UV region. I. Methane and ethane. *Journal of Quantitative Spectroscopy and Radiative Transfer*, *85*, 195–209. https://doi.org/10.1016/S0022-4073(03)00225-5

Chiang, R., Lisman, S., Wong, E., Enright, P., Breckenridge, W., & Jahanshahi, M. (1993). Robust attitude control for Cassini spacecraft flying by Titan. Paper presented at Guidance, Navigation and Control Conference, Monterey, CA. doi: https://doi.org/10.2514/6.1993-3754

Connors, R. E., Roebber, J. L., & Weiss, K. (1974). Vacuum ultraviolet spectroscopy of cyanogen and cyanoacetylenes. *The Journal of Chemical Physics*, *60*(12), 5011–5024. https://doi.org/10.1063/1.1681016

Esposito, L. W., Barth, C. A., Colwell, J. E., Lawrence, G. M., McClintock, W. E., Stewart, A. I. F., et al. (2004). The Cassini Ultraviolet Imaging Spectrograph investigation. *Space Science Reviews*, *115*(1-4), 299–361. https://doi.org/10.1007/s11214-004-1455-8

Ferradaz, T., Bénilan, Y., Fray, N., Jolly, A., Schwell, M., Gazeau, M. C., & Jochims, H. W. (2009). Temperature-dependent photoabsorption cross-sections of cyanoacetylene and diacetylene in the mid- and vacuum-UV: Application to Titan's atmosphere. *Planetary and Space Science*, *57*, 10–22. https://doi.org/10.1016/j.pss.2008.10.005

Foreman-Mackey, D., Hogg, D. W., Lang, D., & Goodman, J. (2013). emcee: The MCMC Hammer. *Publications of the Astronomical Society of the Pacific*, *125*, 306–312. https://doi.org/10.1086/670067

Hörst, S. M. (2017). Titan's atmosphere and climate. *Journal of Geophysical Research: Planets*, *122*, 432–482. https://doi.org.10.1002/2016je005240

Kameta, K., Kouchi, N., Ukai, M., & Hatano, Y. (2002). Photoabsorption, photoionization, and neutral-dissociation cross sections of simple hydrocarbons in the vacuum ultraviolet range. *Journal of Electron Spectroscopy and Related Phenomena*, *123*, 225–238. https://doi.org/10.1016/S0368-2048(02)00022-1

Kammer, J. A., Shemansky, D. E., Zhang, X., & Yung, Y. L. (2013). Composition of Titan's upper atmosphere from Cassini UVIS EUV stellar occultations. *Planetary and Space Science*, *88*, 86–92. https://doi.org/10.1016/j.pss.2013.08.003

Khare, B. N., Sagan, C., Arakawa, E. T., Suits, F., Callcott, T. A., & Williams, M. W. (1984). Optical constants of organic tholins produced in a simulated Titanian atmosphere: From soft X-ray to microwave frequencies. *Icarus*, *60*, 127–137. https://doi.org/10.1016/0019-1035(84)90142-8

Koskinen, T. T., Yelle, R. V., Snowden, D. S., Lavvas, P., Sandel, B. R., Capalbo, F. J., et al. (2011). The mesosphere and lower thermosphere of Titan revealed by Cassini/UVIS stellar occultations. *Icarus*, *216*(2), 507–534. https://doi.org/10.1016/j.icarus.2011.09.022

Lee, L. C. (1980). CN(A 2Πi→X 2Σ+) and CN(B 2Σ+→X 2Σ+) yields from HCN photodissociation. *The Journal of Chemical Physics*, *72*(12), 6414–6421. https://doi.org.10.1063/1.439140

Li, C., Zhang, X., Gao, P., & Yung, Y. (2015). Vertical distribution of C_3-hydrocarbons in the stratosphere of Titan. *The Astrophysical Journal Letters*, *803*, L19–L25. https://doi.org/10.1088/2041-8205/803/2/L19

Li, C., Zhang, X., Kammer, J. A., Liang, M. -C., Shia, R. -L., & Yung, Y. L. (2014). A non-monotonic eddy diffusivity profile of Titan's atmosphere revealed by Cassini observations. *Planetary and Space Science*, *104*, 48–58. https://doi.org/10.1016/j.pss.2013.10.009

Liang, M.-C., Yung, Y. L., & Shemansky, D. E. (2007). Photolytically generated aerosols in the mesosphere and thermosphere of Titan. *The Astrophysical Journal Letters*, *661*, L199–L202. https://doi.org/10.1086/518785

Maltagliati, L., Bézard, B., Vinatier, S., Hedman, M. M., Lellouch, E., Nicholson, P. D., et al. (2015). Titan's atmosphere as observed by Cassini/VIMS solar occultations: CH4, CO and evidence for C2H6 absorption. *Icarus*, *248*, 1–24. https://doi.org/10.1016/j.icarus.2014.10.004

NASA-PDS (2017). Cassini UVIS User's Guide, Planetary Data System (http://pds-rings.seti.org/cassini/uvis/index.html)

Nuth, J. A., & Glicker, S. (1982). The vacuum ultraviolet spectra of HCN, C_2N_2, and CH_3CN. *Journal of Quantitative Spectroscopy and Radiative Transfer*, *28*, 223–231. https://doi.org/10.1016/0022-4073(82)90025-5

Pantos, E., Philis, J., & Bolovinos, A. (1978). The extinction coefficient of benzene vapor in the region 4.6 to 36 eV. *Journal of Molecular Spectroscopy*, *72*, 36–43. https://doi.org/10.1016/0022-2852(78)90041-3

Pilinski, E. B., & Lee, A. Y. (2009). Pointing-stability performance of the Cassini spacecraft. *Journal of Spacecraft and Rockets*, *46*, 1007–1015. https://doi.org/10.2514/1.41675

Shemansky, D. E., & Liu, X. (2012). Saturn upper atmospheric structure from Cassini EUV and FUV occultations. *Canadian Journal of Physics*, *90*, 817–831. https://doi.org/10.1139/p2012-036

Shemansky, D. E., Stewart, A. I. F., West, R. A., Esposito, L. W., Hallett, J. T., & Liu, X. (2005). The Cassini UVIS stellar probe of the Titan atmosphere. *Science*, *308*, 978–982. https://doi.org/10.1126/science.1111790

Vervack, R. J., Sandel, B. R., & Strobel, D. F. (2004). New perspectives on Titan's upper atmosphere from a reanalysis of the Voyager 1 UVS solar occultations. *Icarus*, *170*, 91–112. https://doi.org/10.1016/j.icarus.2004.03.005

Willacy, K., Allen, M., & Yung, Y. (2016). A new astrobiological model of the atmosphere of Titan. *The Astrophysical Journal*, *829*, 79–89. https://doi.org/10.3847/0004-637X/829/2/79

Wu, C. Y. R., Chen, F. Z., & Judge, D. L. (2001). Measurements of temperature-dependent absorption cross sections of C_2H_2 in the VUV-UV region. *Journal of Geophysical Research*, *106*, 7629–7638. https://doi.org/10.1029/2000JE001292

Wu, C. Y. R., Chen, F. Z., & Judge, D. L. (2004). Temperature-dependent photoabsorption cross sections in the VUV-UV region: Ethylene. *Journal of Geophysical Research*, *109*, E07S15. https://doi.org/10.1029/2003JE002180